Geophys. J. Int. (2008) **173,** 577–592 doi: 10.1111/j.1365-246X.2008.03748.x

Crack density tensor inversion for analysis of changes in rock frame architecture

Stephen A. Hall,[1] J-Michael Kendall,[2] Jamie Maddock[3] and Quentin Fisher[3]

[1] *Laboratoire 3S-R, CNRS/Grenoble Universities, Grenoble, France. E-mail: stephen.hall@hmg.inpg.fr*
[2] *Department of Earth Sciences, University of Bristol, UK*
[3] *School of Earth Sciences, University of Leeds, UK*

Accepted 2008 January 29. Received 2008 January 29; in original form 2006 December 15

SUMMARY

This paper presents a development of the use of multi-axial ultrasonic data for the quantification of extrinsic, crack or grain-contact induced elastic anisotropy in core samples with application to a UKCS oil field. An approach for inversion of multi-axial velocity measurements is presented, which extends the previous work by Sayers (2002) for the determination of second- and fourth-order crack density tensors from inversion of multi-axial ultrasonic velocity data. The extensions to the inversion approach provide improved consideration of data uncertainties, by using all available *P*- and *S*-wave data and also permit the inclusion of an orthorhombic background anisotropy in the inversion [e.g. due to intrinsic lattice preferred orientation(LPO) effects]. The latter aspect leads to estimates of the extrinsic anisotropy, that is, the quantified crack density tensors, that are 'unpolluted' by the effects of the intrinsic anisotropy, thus permitting extrinsic and intrinsic anisotropies to be distinguished.

For the samples considered, the extrinsic crack-induced anisotropy is strong relative to that of the intrinsic LPO effects, and the pre-dominant crack-set is commonly aligned parallel to the depositional fabric (which is generally horizontal). However, the LPO and extrinsic anisotropies are in general aligned, which indicates a linked origin. Furthermore, a strong correlation is observed between the degree of VTI anisotropy and the modal content of micas in the samples, which cannot be explained solely by the LPO effect. In fact, it is shown that increased horizontal (grain parallel) crack densities are associated with higher mica content. These horizontal cracks in the mica-rich samples often show moderate-to-strong variations in crack density with loading that might be detected *in situ* with non-hyperbolic moveout. Additionally, three samples show significant pressure sensitivity of the vertical crack sets indicating that loading-induced azimuthal anisotropy might also exist in some layers *in situ* and be detectable using azimuthal AVO type analyses.

Analysis of the fourth-order crack density tensor allows insight into the relative sizes of the normal and tangential crack compliances, B_N and B_T. For one case it is found that $B_N \geq B_T$ (i.e. the crack-sets are more compliant in compression than in shear). For another sample $B_N < B_T$; this sample had been cleaned prior to the analysis, which appears to facilitate shear in the cracks. This conclusion may have significant implications for the use of analogue samples acquired at the surface where organic products, which lead to the reduced shear compliance, are not present.

Key words: Microstructure; Seismic anisotropy.

1 INTRODUCTION

Seismic anisotropy in sedimentary rocks arises due to a number of mechanisms over a range of length scales; therefore, it is difficult to interpret the cause of anisotropy using field-scale seismic data. At the smallest scale, petrofabric analyses can be used to estimate ansisotropy due to the preferred orientation of crystals (lattice preferred orientation, LPO) (e.g. Valcke *et al.* 2006). At the hand-specimen scale, additional contributions to anisotropy exist that can be generally described as shape preferred orientation (SPO) effects. These include the preferred alignment of microcracks or thin pores and grain-boundary contacts (e.g. Crampin 1984), which are inherently load-dependent. Finally, small-scale layering or a non-random distribution of mineral phases can also generate anisotropy; these two effects are less load-dependent than

those due to microcracks, compliant pores or grain boundaries. Linked petrofabric analysis and laboratory measurements of velocities might be used to help untangle the relative contributions from these LPO and SPO mechanisms. Furthermore, laboratory measurements of ultrasonic velocities as a function of confining pressure can be used to assess the load-dependence of the anisotropy (e.g. Nur & Simmons 1969). Such knowledge of anisotropy at the hand-specimen scale is in turn useful for interpreting field-scale seismic observations. At the field-scale, the key mechanism of interest is often the preferred orientation of large-scale fractures, which might provide important pathways for fluid flow in reservoirs. Such fractures can generate anisotropy in field-scale seismic data, but this will not be evident in core-scale data. Hence, one can endeavour to constrain the causes of observed anisotropy by first determining the LPO anisotropy through petrofabric measurements, then asessing the stress-dependent and stress-independent SPO anisotropy using core-scale ultrasonic measurements and finally interpreting the longer-wavelength anisotropy using field-scale seismic observation.

This paper concentrates on the characterization of the grain-scale LPO and SPO anisotropy for a suite of core-samples from a siliciclastic UKCS oil reservoir. An approach is presented that utilizes petrofabric analyses and inversion of multi-axial velocity measurements using a crack density tensor description. This 'crack' description includes the contributions due to all the compliant crack-like features present at the grain-scale (microcracks, grain-boundary contacts, etc.) and accomodates the influence of their filling materials (clays, etc.) through their overall effect on the crack compliances. This approach extends the developments of Sayers (2002) to utilize more of the available velocity data and provide illumination of more components of the fourth-order crack density tensor, plus to allow the inclusion of an (*a priori* determined) intrinsic, orthorhombic LPO anisotropy. The main objective is separation of the intrinsic and extrinsic components of the anisotropy, which in turn allows characterization of the extrinsic fabrics with quantitative descriptions of grain-boundary/crack architecture and the variation under loading. After a brief overview of the subject, the paper proceeds by outlining the theoretical background to the data inversion strategy. Following this overview, the UKCS oil field core samples and ultrasonic data are described before presenting the results of the inversions for the second- and fourth-order crack density tensors. Finally, the results are discussed on the basis of the possible causes of the anisotropy and the implications for reservoir characterization.

1.1 Characterization of seismic anisotropy in rocks

Microcracks, thin pores and grain-boundary contacts represent highly compliant features that can produce significant anisotropy in the elastic properties of rocks that can vary considerably under loading. There has been extensive work on the characterization of such crack-induced anisotropy and its load-dependence using experimental observations (e.g. Nur & Simmons 1969; King *et al.* 1995; Sayers & Kachanov 1995; Sayers 2002; Gueguen & Schubnel 2003), theoretical models of the structural (e.g. Budiansky & O'Connell 1976; Hoenig 1978; Hudson 1980, 1981; Sayers & Kachanov 1991, 1995; Schoenberg & Sayers 1995; Hudson & Liu 1999; Sayers 2002) and also load-dependent aspects (e.g. Nur 1971; Toksoz *et al.* 1976) . Alternatively load-dependent effects might be considered in terms of non-linear- or acousto-elasticity, which in essence ignores the microscale origins of the anisotropy and aims to describe the observed macroscopic variations with stress; see Rasolofosaon (1998) for a good summary. The effect of LPO fabrics on elastic properties of rocks has primarily been investigated in relation to studies of the deep Earth (e.g. Mainprice 1990), for example, to map olivine alignment and thus mantle flow (e.g. Blackman & Kendall 1997). Fewer studies exist on the characterization of LPO effects in sedimentary rocks (examples include Cholach & Schmitt 2003; Valcke *et al.* 2006). In addition, whereas the theoretical framework for considering cracks in an arbitrarily anisotropic matrix has long been established (e.g. Kachanov 1980; Sayers & Kachanov 1991, 1995), studies that consider both the extrinsic and intrinsic effects are limited. Recent work by Han *et al.* (2004) considered such a problem for ophiolite rocks.

Full characterization of velocity anisotropy in laboratory rock specimens requires the impractical acquisition of a large number of velocity measurements along many different axes (e.g. by using spherical samples; Rasolofosaon *et al.* 2000). Desk-top (unconfined) measurements are a relatively simple means to achieve good characterization of velocity anisotropy or heterogeneity, for example, through circumferential velocity analysis (e.g. Hall *et al.* 2000) or even tomography (e.g. Debski & Young 1999). However, acquiring multi-axis velocity measurements under pressure is challenging. Standard rock-mechanics apparatus with velocity measurement capabilities are usually designed with transducers mounted in the piston allowing ultrasonic wave propagation along the core axis. Even with both *P*- and *S*-wave transducers, this does not provide sufficient data to characterize anisotropy. A solution to this problem is to install sensors on the surface of the sample, through the sample-jacket (e.g. Stanchits *et al.* 2003), but this requires a more complex set-up (e.g. to acquire sufficient *P*- and *S*-wave data requires a large number of transducers but with only a finite surface area available). King *et al.* (1995) overcame a number of problems by developing a poly-axial loading cell for cubic samples, in which both *P*- and *S*-wave ultrasonic transducers could be placed on all six faces; this is however a specialized apparatus. Han *et al.* (2004) utilized an alternative approach whereby multi-axial measurements were achieved in a standard pressure-cell, with *P*- and *S*-wave transducers mounted only in the piston, by using specimens cut along different axes relative to the rock fabric. Such an approach was adopted for the velocity measurements considered in this work, using a pressure cell developed at the University of Manchester, UK.

For any of the methods of ultrasonic velocity measurements described above, characterization of the anisotropy is still in general limited. Therefore, an assumption is normally made that the anisotropy in the sample is of higher symmetry, such as transversely isotropic, which allows the assumed anisotropy to be characterized with fewer measurements. For the case of transverse isotropy only five measurements are needed: *P*- and *S*-wave measurements along the principal axes (parallel and perpendicular to the symmetry plane) and an off-axis *P*-wave measurement (normally at 45° to the other measurements) (e.g. Lo *et al.* 1986; Sayers & Kachanov 1995; Hornby 1998). Transverse isotropy is often thought to be a good assumption for many sedimentary rocks, and in particular shales, due to the alignment of platy phylosilicates

during deposition, compaction and diagenizis under the influence of gravity. Sandstones, however, may show more complex symmetries as a result of higher-activity depositional environments and lower platy mineral content. Additionally, the effects of loading, leading to cracking and changes in grain-boundary configuration, are likely to be more complex than in shales due to the larger aspect ratio grains. In this work the anisotropy of the rock samples is assumed to be at most orthorhombic, which requires *P*- and *S*-wave velocity measurements along the three principal axes, plus off-axis *P*-wave velocities within the symmetry planes.

Interpretation of the variations (anisotropic or otherwise) in ultrasonic velocities with loading commonly considers empirical descriptions of the observed logarithmic trends. To achieve a more quantitative analysis with multi-axial velocity measurements and to assess changes in the crack architecture under loading, Sayers (2002) presented an inversion strategy based around the previous developments of Sayers & Kachanov (1991, 1995). This approach allows the determination of crack density tensors that describe multiple populations of cracks or crack-like porosity. In fact, this approach can be used to describe any population of cracks if they have equal normal and tangential compliances, as is discussed in the following section.

2 METHOD FOR CRACK DENSITY TENSOR INVERSION

This section outlines an approach for estimating the second- and fourth-order crack density tensors, α_{ij} and β_{ijkl}, from multi-axial ultrasonic velocity measurements. The approach is based on that presented by Sayers (2002) with extension to take into account the intrinsic anisotropy, using a pre-determined orthorhombic background medium, which allows the intrinsic effects to be separated out of the analysis [The samples considered in this work show only small non-orthogonal terms in the LPO stiffness tensors, as determined using petrofabric analyses, so the assumption of an orthorhombic (LPO) background is reasonable]. In addition, the inversion approach suggested here differs from that of Sayers (2002) in that all available data are utilized in both the initial inversion for α_{ij} and the second stage inversion for β_{ijkl}. This difference in approach better captures the data uncertainty and also allows a more complete assessment of the β_{ijkl} tensor. The following first presents the theoretical background to the problem before describing the inversion strategy.

2.1 Theoretical background

Following Sayers & Kachanov (1991, 1995) and Sayers (2002), the elastic compliance, s_{ijkl}, of a rock can be described by,

$$s_{ijkl} = s^0_{ijkl} + \Delta s_{ijkl}. \tag{1}$$

Here s^0_{ijkl} is the compliance of the rock matrix, which will be the aggregate anisotropic compliance of all the constituent grains. At the core scale Δs_{ijkl} can be considered as describing the additional compliance due to the presence of small discontinuities such as cracks or grain-boundary contacts. It is noted that for scales larger than that of a core sample, Δs_{ijkl} will include further compliant components, for example relating to wider-spaced fractures. However, as such components are not generally present in core specimens, laboratory measurements of core-sample elastic compliances can be considered as just being the summation of the intrinsic, crystallographic, s^0_{ijkl} and extrinsic, crack or grain contact, Δs_{ijkl}.

Following Sayers & Kachanov (1991, 1995) and Sayers (2002), Δs_{ijkl} can be described in terms of second- and fourth-order 'crack density tensors', α_{ij} and β_{ijkl},

$$\Delta s_{ijkl} = \frac{1}{4}\left(\delta_{ik}\alpha_{jl} + \delta_{il}\alpha_{jk} + \delta_{jk}\alpha_{il} + \delta_{jl}\alpha_{ik}\right) + \beta_{ijkl}, \tag{2}$$

where δ_{ij} is the Kronnecker delta. For a distribution of r planar discontinuities with surface areas $A^{(r)}$ and surface-normal vectors $n_i^{(r)}$ in a volume V, these crack density tensors can be defined in terms of two crack compliance terms that describe the additional normal and tangential compliances, B_N and B_T, due to each discontinuity,

$$\alpha_{ij} = \frac{1}{V}\sum_r B_T^{(r)} n_i^{(r)} n_j^{(r)} A^{(r)}, \tag{3}$$

$$\beta_{ijkl} = \frac{1}{V}\sum_r \left(B_N^{(r)} - B_T^{(r)}\right) n_i^{(r)} n_j^{(r)} n_k^{(r)} n_l^{(r)} A^{(r)}, \tag{4}$$

(Sayers & Kachanov 1991, 1995; Sayers 2002). B_N and B_T characterize the normal and tangential displacement discontinuities due to normal and tangential tractions acting upon the cracks faces. Therefore, α_{ij} and β_{ijkl} can be thought of as characterizing the cumulative magnitude and orientation distribution function of the additional normal and shear compliances due to all the compliant discontinuities present in a sample, plus the relative ease to undergo shear or opening along the different orientations. For the special case where for all the cracks $B_N = B_T$, it follows that $\beta_{ijkl} = 0$. In this case, any set of cracks can be represented by three orthogonal effective 'scalar' crack sets that are fully described by the second order crack density tensor, α_{ij}, which has principal axes defined by the three scalar crack densities, α_{11}, α_{22} and α_{33} (Sayers & Kachanov 1995). Δs_{ijkl} will thus be orthotropic and aligned with α_{ij}. Deviations from such a scalar crack model, that is, for $B_N \neq B_T$, will give rise to non-zero values of β_{ijkl}; however, Sayers & Kachanov (1995) and Sayers (2002) argue that in most cases, the magnitude of β_{ijkl} will be small (For example for the case, of dry penny-shaped cracks in a sandstone, Sayers & Kachanov (1995) point out that B_N and B_T are approximately equal as $B_N/B_T = 1 - \nu_0/2 \to 1$ since the Poisson's ratio is small, ≈0.1–02; see below). These observations permit

the deviations from orthotropy (i.e. non-zero β_{ijkl}) to be considered as perturbations to a scalar crack model, which leads to the two-stage inversion approach discussed later.

It is noted that the trace of α_{ij} normalized by an appropriate factor h (as given below for open, planar penny-shaped cracks, or an equivalent adapted for the specific crack conditions) is the commonly used crack density tensor $\frac{Na^3}{V}$, for N cracks of diameter a in a volume V (Gueguen & Schubnel 2003). The trace of β_{ijkl} is similarly related to this crack density scalar but its definition, for the case below, also involves a term relating to the crack aperture and the moduli of crack fill.

In the results presented later in this paper, the crack density tensors are presented in a normalized form. In this case, the normalizing factor, h, used is defined from the equations for B_N and B_T of Sayers & Kachanov (1995) corresponding to the case of open, planar, penny-shaped cracks,

$$B_N = \frac{16\left(1-\nu_0^2\right)a}{3\pi E_0},\ B_T = \frac{32\left(1-\nu_0^2\right)a}{3\pi E_0(2-\nu_0)}, \tag{5}$$

where a is the diameter of the cracks embedded in a dry, isotropic rock with Young's modulus E_0 and Poisson's ratio ν_0. On the basis of these equations, the normalizing factor for the crack density terms is defined,

$$h = \frac{3E_0(2-\nu_0)}{32(1-\nu_0^2)}, \tag{6}$$

(this is equivalent to the normalizing parameter of Sayers & Kachanov 1995; Gueguen & Schubnel 2003). For an anisotropic rock matrix with orthotropic symmetry this normalizing factor must be defined for each of the three principal symmetry directions, $i = 1, 2, 3$,

$$h_i = \frac{3E_i(2-\nu_i)}{32\left(1-\nu_i^2\right)}, \tag{7}$$

where the Young's moduli are the values in the three principal directions and the Poisson's ratio are based on the averages of the shear compliances along the principal axes: $\nu_1 = (-S^0_{12} - S^0_{13})/(2S^0_{11})$; $\nu_2 = (-S^0_{21} - S^0_{23})/(2S^0_{22})$; $\nu_3 = (-S^0_{31} - S^0_{32})/(2S^0_{33})$. (Note that here, and in the following, the reduced, Voigt, form of the tensors s_{ijkl} and c_{ijkl} are used; denoted by S_{ij} and C_{ij}, respectively.)

The normalization by h allows the results to be presented in a coherent form; however, it should be noted that the approach does not in fact consider any idealized representation of the cracks (other than that they are thin and compliant). Subsequent interpretation of the 'real' crack density, from the normalized values (which are essentially just compliances), can only be made in terms of some idealized crack geometry, for example, ellipsoids or pennies. Such interpretation will however be subject to a non-uniqueness and a trade-off between aspect ratio and crack density (for the above case of the open, planar, penny-shaped cracks, the given crack densities are correct for the case of zero aspect ratio; see Sayers & Kachanov 1995).

With the assumption of scalar cracks ($B_N = B_T$, $\beta_{ijkl} = 0$), Sayers (2002) presented a set of equations to describe the elastic constants of the cracked medium and that can also be used to determine the crack density tensor, α_{ij}, from ultrasonic measurements along the principal axes. These equations are generalized below for an anisotropic background medium with orthorhombic symmetry aligned with the crack anisotropy (this derivation follows simply from equations (A14) to (A32) in the appendix of Sayers 2002). Additionally, the equations are given with the fourth-order crack density tensor terms, which were omitted in Sayers (2002), as these will be used later. Thus the non-zero elements of the upper-triangle of the stiffness tensor for an orthorhombic background and orthotropic crack assemblage, using the condensed Voigt notation, are,

$$C_{11} = \left[\left(S^0_{23}+\beta_{2233}\right)^2 - \left(S^0_{22}+\alpha_{22}+\beta_{2222}\right)\left(S^0_{33}+\alpha_{33}+\beta_{3333}\right)\right]/D, \tag{8}$$

$$C_{22} = \left[\left(S^0_{13}+\beta_{1133}\right)^2 - \left(S^0_{11}+\alpha_{11}+\beta_{1111}\right)\left(S^0_{33}+\alpha_{33}+\beta_{3333}\right)\right]/D, \tag{9}$$

$$C_{33} = \left[\left(S^0_{12}+\beta_{1122}\right)^2 - \left(S^0_{11}+\alpha_{11}+\beta_{1111}\right)\left(S^0_{22}+\alpha_{22}+\beta_{2222}\right)\right]/D, \tag{10}$$

$$C_{12} = \left[\left(S^0_{12}+\beta_{1122}\right)\left(S^0_{33}+\alpha_{33}+\beta_{3333}\right) - \left(S^0_{13}+\beta_{1133}\right)\left(S^0_{23}+\beta_{2233}\right)\right]/D, \tag{11}$$

$$C_{13} = \left[\left(S^0_{13}+\beta_{1133}\right)\left(S^0_{22}+\alpha_{22}+\beta_{2222}\right) - \left(S^0_{12}+\beta_{1122}\right)\left(S^0_{23}+\beta_{2233}\right)\right]/D, \tag{12}$$

$$C_{23} = \left[\left(S^0_{23}+\beta_{2233}\right)\left(S^0_{11}+\alpha_{11}+\beta_{1111}\right) - \left(S^0_{12}+\beta_{1122}\right)\left(S^0_{13}+\beta_{1133}\right)\right]/D, \tag{13}$$

$$C_{44} = \left(S^0_{44}+\alpha_{22}+\alpha_{33}+4\beta_{2233}\right)^{-1}, \tag{14}$$

$$C_{55} = \left(S^0_{55}+\alpha_{11}+\alpha_{33}+4\beta_{1133}\right)^{-1}, \tag{15}$$

$$C_{66} = \left(S^0_{66}+\alpha_{11}+\alpha_{22}+4\beta_{1122}\right)^{-1}, \tag{16}$$

where,

$$\begin{aligned} D = {} & \left(S^0_{11}+\alpha_{11}+\beta_{1111}\right)\left(S^0_{23}+\beta_{2233}\right)^2 + \left(S^0_{22}+\alpha_{22}+\beta_{2222}\right)\left(S^0_{13}+\beta_{1133}\right)^2 \\ & + \left(S^0_{33}+\alpha_{33}+\beta_{3333}\right)\left(S^0_{12}+\beta_{1122}\right)^2 - 2\left(S^0_{12}+\beta_{1122}\right)\left(S^0_{13}+\beta_{1133}\right)\left(S^0_{23}+\beta_{2233}\right) \\ & - \left(S^0_{11}+\alpha_{11}+\beta_{1111}\right)\left(S^0_{22}+\alpha_{22}+\beta_{2222}\right)\left(S^0_{33}+\alpha_{33}+\beta_{3333}\right). \end{aligned} \tag{17}$$

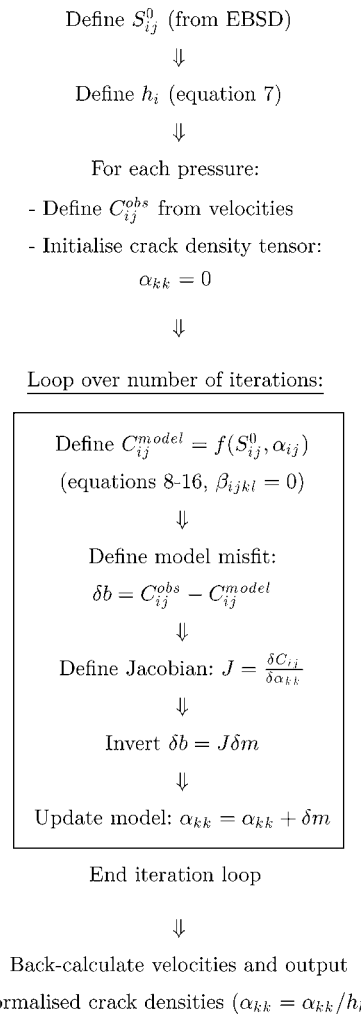

Figure 1. Flow chart for inversion procedure for scalar cracks ($B_N = 0$, $B_T = 0 \therefore \beta_{ijkl} = 0$). In the inversion procedure, the model vector, m, is the vector $\{\alpha_{11}, \alpha_{22}, \alpha_{33}\}$ and the Jacobian describes the variation of C_{ij} with respect to α_{ij}. (Note, α_{kk} does not involve summation over k.)

2.2 Outline of inversion strategy

The above equations can be used to invert the multi-axial velocity data to derive the crack density tensors of Sayers (2002). The approach involves two steps, as described below. The first step derives the α_{ij} terms for assumed scalar cracks (either using just the principal *P*-wave data or using all the data) and the second step derives β_{ijkl}, which is considered as a perturbation to the scalar crack model.

2.2.1 Step 1: Inversion for α_{ij}

Fig. 1 outlines the inversion procedure to derive the three non-zero components of α_{ij}(α_{11}, α_{22} and α_{33}) based on the assumption of scalar cracks ($B_N = B_T \therefore \beta_{ijkl} = 0$). The inversion uses eqs (8)–(10) when considering just the principal *P*-wave data and (8)–(16) when all the data are used. In both cases, the β_{ijkl} are assumed to be zero, in this initial step. The inversion uses the appropriate set of simultaneous eqs (8)–(10) or (8)–(16) and background elasticities (the S^0_{ij} terms from the petrofabric analyses) to relate the model vector, containing the three terms α_{11}, α_{22} and α_{33}, to the data vector of the $C^{\rm obs}_{ij}$, which are the elastic properties determined from the measured velocities and density. The inversion is performed using an iterative, Newton–Raphson approach (Press *et al.* 1992). The available velocity data, in this example, allow the definition of seven components of the observed stiffness tensor, $C^{\rm obs}_{ij}$: $C^{\rm obs}_{11}$, $C^{\rm obs}_{22}$, $C^{\rm obs}_{33}$, $C^{\rm obs}_{13}$, $C^{\rm obs}_{44}$, $C^{\rm obs}_{55}$ and $C^{\rm obs}_{66}$. Thus the Jacobian matrix (step 6/7 in Fig. 1), which describes the variation of $C^{\rm model}_{ij}$ as a function of variations in the three non-zero components of α_{ij}, is 7×3 (unless only a subset of data, such as just the *P*-wave data, are used, in which case the Jacobian is reduced accordingly). It is assumed that the principal axes of the background anisotropy and the crack anisotropy are coincident and aligned with the axes of the velocity measurements.

2.2.2 Step 2: Perturbation analysis for β_{ijkl}

Fig. 2 shows a flow diagram for the perturbation-based inversion to derive components of β_{ijkl} based on a previously derived set of α_{11}, α_{22} and α_{33} (from step 1, above). It is assumed that all of the deviations of the velocities backcalculated using the prior scalar-crack model, from

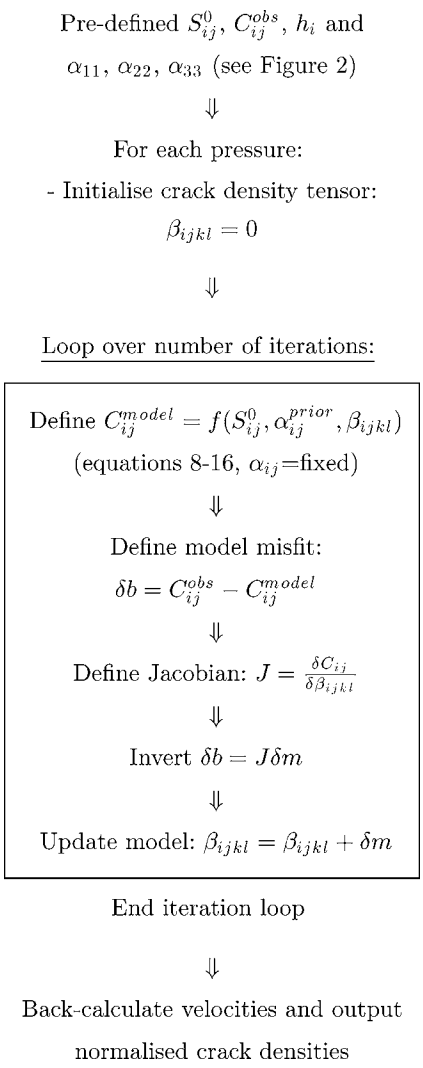

Figure 2. Flow chart for inversion procedure for non-scalar cracks based on perturbation to scalar crack model (pre-derived, fixed α_{ij} and inverting for β_{ijkl} with data residuals). In the inversion procedure, the model vector, m, is the vector the illuminated elements of β_{ijkl} and the Jacobian describes the variation of C_{ij} with respect to β_{ijkl}.

the measured velocities, are due to the influence of β_{ijkl} (i.e. due to unequal B_N and B_T). Thus eqs (8)–(17) are used with the S_{ij}^0, as above, and fixed values of α_{11}, α_{22} and α_{33}, from step 1 of the inversion. With the available velocity data, the components of β_{ijkl} that can be resolved are β_{1111}, β_{2222}, β_{3333}, β_{2233}, β_{1133} and β_{1122} (thus the Jacobian matrix, in steps 5/6 of Fig. 2, is 7×6).

2.3 Extensions to Sayers (2002)

Sayers (2002) used the isotropic-background version of eqs (14)–(16), with $\beta_{ijkl} = 0$ (i.e. for scalar cracks, $B_N = B_T$), to determine the second-order crack density tensor from shear wave velocity measurements along the principal axes. Subsequently the fourth order crack density tensor was determined by a perturbation approach, as above. In this current work, all the eqs (8)–(17) (with the β_{ijkl} terms set to zero) that correspond to the available data are used in an iterative solution for α_{11}, α_{22} and α_{33} (using a Newton–Raphson type approach). This permits the analysis to be carried out in the absence of appropriate shear wave data or to include all data and thus to achieve a best-fit result. Such an approach is more appropriate since the data uncertainty is better accounted for than in the approach discussed by Sayers (2002). Additionally, it is not pre-dictated which terms of β_{ijkl} are more important; there is an inherent assumption in the original Sayers (2002) approach that the misfit from the scalar crack model is just due to the *P*-wave terms of β_{ijkl}(β_{1111}, β_{2222} and β_{3333}) and that the shear-related terms are negligible. In this current work, more data are available and additional degrees of freedom are left open by using a more general iterative derivation of the scalar crack model.

3 CORE SAMPLES, ULTRASONIC DATA AND LPO QUANTIFICATION

The core samples considered in this work originate from different levels in two wells in a UKCS field where the lithologies are basically sandstones. Sample *A* is from a different well to the other eight. Fig. 3 shows the modal proportions of the constituent minerals (and

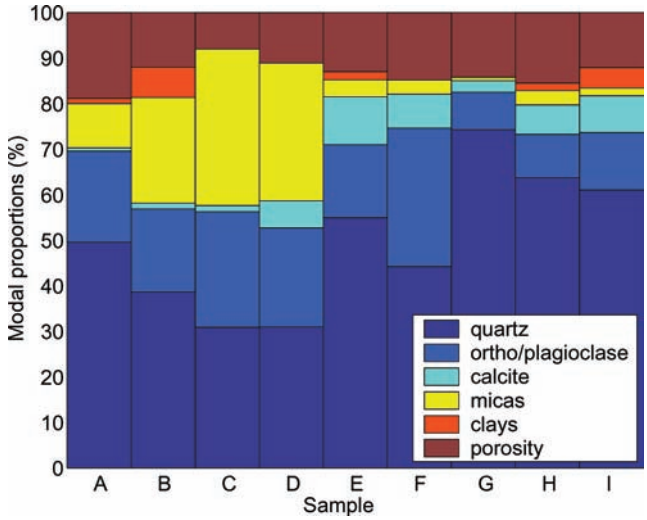

Figure 3. Histogram of the modal proportions of the constituent mineral (and porosity) of each of the samples as determined by QXRD (and by mercury impregnation for the porosity).

porosity) for each of the samples studied. The principal constituent of the samples is quartz, but in varying proportions. A key variability between the samples is the mica content, which is greatest in Samples *B*, *C* and *D*. Some of the samples (*E* and *G*) were cleaned prior to the velocity analysis, which resulted in the washing-out of most of the organic constituents and perhaps other material (e.g. fine-scale clays). Analysis of these samples may provide some insight into factors that control the crack compliances, other than the cracks themselves.

For each core sample, four cylindrical specimens (25.4 mm diameter, 40 mm long) were made for the velocity measurements, one vertical (perpendicular to bedding: Z–x_3) and two, mutually orthogonal, in the plane of the bedding (X–x_1; Y–x_2). A final specimen was cut at 45° to the Z axis in the X-Z plane. Shear and compressional wave velocity measurements were made parallel to the axis of each of the four specimens from each core sample at different hydrostatic pressures (in the range 0–50 MPa). Thus, assuming that the elastic symmetry axes are aligned with the test configuration, the 'observed' elastic moduli are defined, for each pressure, as $C_{11}^{\mathrm{obs}} = \sqrt{\frac{v_{p11}}{\rho}}$, $C_{22}^{\mathrm{obs}} = \sqrt{\frac{v_{p22}}{\rho}}$, $C_{33}^{\mathrm{obs}} = \sqrt{\frac{v_{p33}}{\rho}}$, $C_{44}^{\mathrm{obs}} = \sqrt{\frac{v_{s23}}{\rho}}$, $C_{55}^{\mathrm{obs}} = \sqrt{\frac{v_{s13}}{\rho}}$ and $C_{66}^{\mathrm{obs}} = \sqrt{\frac{v_{s12}}{\rho}}$ (the first velocity subscript indicates the direction of propagation and the second the polarization). In most cases two equivalent shear velocity measurements were available (e.g. $v_{s_{12}}$ and $v_{s_{21}}$), so the average of the two values was used. The off-axis stiffnesses (C_{13}^{obs}) were derived using the calculated C_{11}^{obs}, C_{33}^{obs} and C_{44}^{obs} with the off-axis P-wave velocity measurement $v_{p13}^{45^\circ}$ and the equations given by Hornby (1998),

$$C_{13}^{\mathrm{obs}} = -C_{44}^{\mathrm{obs}} + \sqrt{\left[\left(C_{11}^{\mathrm{obs}} + C_{44}^{\mathrm{obs}} - 2\rho v_p^{45^2}\right)\left(C_{33}^{\mathrm{obs}} + C_{44}^{\mathrm{obs}} - 2\rho v_p^{45^2}\right)\right]}. \tag{18}$$

Quantification of the aggregate mineral constituents and the intrinsic anisotropic elasticity due to their alignment (LPO effects) was achieved using quantitative X-ray diffraction (QXRD) and electron backscattered diffraction (EBSD) analysis, respectively (Maddock *et al.* 2004). QXRD allows identification of the constituent minerals and their modal proportions (Hillier 1999). EBSD measurements were used to quantify the orientation distribution functions for each of the different mineral constituents. The bulk porosities of the samples were determined using mercury impregnation. These data were incorporated, by Voigt–Reuss–Hill averaging, with known anisotropic mineral elasticities to provide a prediction, for each sample, of the LPO contribution to the aggregate anisotropic stiffness tensor. These predictions can thus be used as input to the inversion procedure, described earlier, as *a priori* information on the anisotropic stiffnesses related to only the LPO effects, assuming the absence of cracks, grain boundaries, etc., but including isotropic (equant) porosity. Integration of these LPO effects into the analysis allows for correct determination of the extrinsic anisotropy, separated from the LPO contribution. The following section demonstrates this analysis for the UKC*S*-reservoir core samples.

4 RESULTS

Fig. 4 shows the velocity versus pressure data for each sample and, since in some cases the data suite was incomplete, Table 1 summarizes the available data (and compares the velocities, for the principal directions, calculated from the LPO data and those measured at high pressure). The results of the inversion of these data for α_{ij} are first presented for the approach using just the principal P-wave data (Fig. 5), and subsequently using, in addition, the less well-defined shear wave and off-axis measurements (Fig. 6) to assess how the additional data may influence the results. Subsequently, the inversion results for β_{ijkl} for two representative samples are shown in Fig. 7.

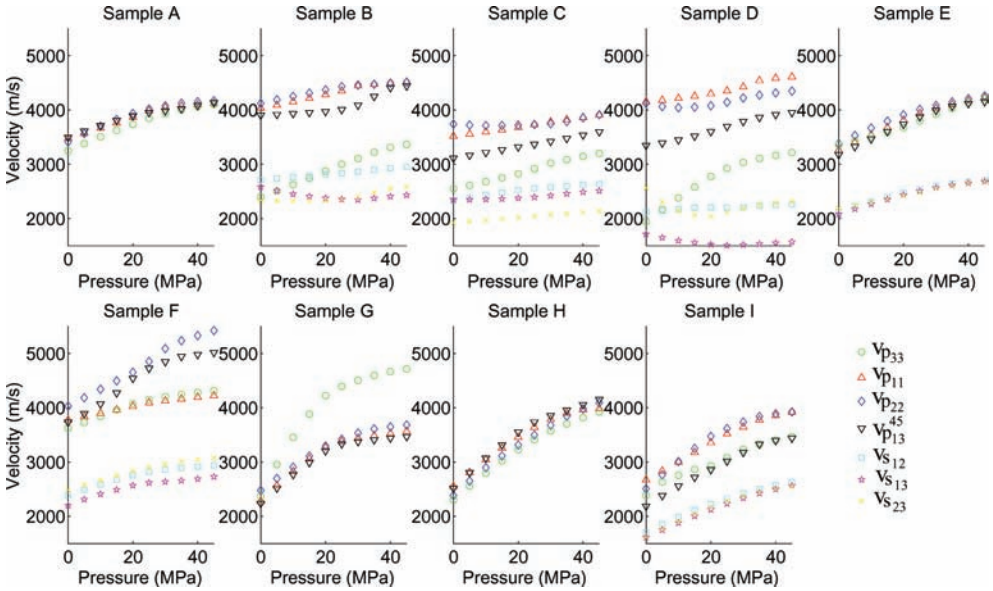

Figure 4. Measured velocities for each sample. (Green circle – $v_{p_{33}}$, red triangle – $v_{p_{11}}$, blue diamond – $v_{p_{22}}$, black inverted triangle – $v_{p_{13}}^{45^\circ}$, cyan square – $v_{s_{12}}$, magenta star – $v_{s_{13}}$, yellow cross – $v_{s_{23}}$.)

Table 1. Summary of LPO (first line for each entry) and high-pressure (50 MPa) ultrasonic velocities (m s^{-1}). A '–' indicates that no measurements are available.

Sample	$v_{p_{11}}$	$v_{p_{22}}$	$v_{p_{33}}$	$v_{s_{12}}$	$v_{s_{13}}$	$v_{s_{23}}$	$v_{p_{13}}^{45^\circ}$
A	5517	5502	5203	3512	3412	3361	5366
	4152	4177	4125	–	–	–	–
B	5881	5868	5238	3665	3362	3317	5583
	4540	4538	3421	2973	2452	2583	4457
C	6165	6146	5250	3792	3338	3287	5753
	3952	2987	3239	2650	2529	2157	3724
D	6057	6041	5244	3713	3308	3261	5687
	4636	4369	3284	2264	1603	2299	3988
E	5693	5682	5550	3593	3579	3533	5622
	4275	4285	4260	2720	2708	2698	4168
F	5574	5549	5426	3452	3464	3401	5501
	4252	5433	4337	2963	2779	3104	5075
G	5608	5605	5543	3702	3725	3683	5575
	3599	3714	4749	–	–	–	–
H	5603	5599	5479	3623	3611	3571	5542
	3997	4173	3996	–	–	–	–
I	5673	5666	5584	3627	3640	3596	5629
	3972	3954	3546	2672	2615	2588	3482

4.1 Step 1: Inversion for α_{ij} assuming scalar cracks ($B_N = B_T \therefore \beta_{ijkl} = 0$)

Fig. 5 presents the predictions of α_{ij}, as functions of hydrostatic load, for each sample based on just the three principal *P*-wave velocities. Fig. 6 shows the inversion results as determined using all the velocity data. In each case, the backcalculated velocities are compared with the measured velocities and sample-specific observations are presented in Table 2.

For the first set of results (Fig. 5), derived from just the principal *P*-wave data, a good fit of the backcalculated velocities to the three measured velocities used in the inversion is seen. This is as would be expected, but there is a significant deviation of the modelled and data velocities for the unused data (the shear velocities and $v_{p_{13}}^{45^\circ}$). When all the data are used in the inversion (Fig. 6), little change is seen in the derived α_{ij} values or their variation with pressure, except for α_{33} in samples *B*, *C* and *D*. In general it seen that the fit of the backcalculated velocities to the data is improved (a small residual misfit of the *P*-wave velocities appears, which is not surprising as there will be some uncertainty due to data errors and the possible influence of β_{ijkl}). Furthermore, it can be seen that the scalar-crack model provides reasonable results, particularly at higher pressures. Some deviations exist that may indicate there is an influence due to the fourth-order tensor terms. In most cases the match of the model and the data for $v_{p_{13}}^{45^\circ}$ is the worst, even when all the data are used in the inversion. This poor misfit could be

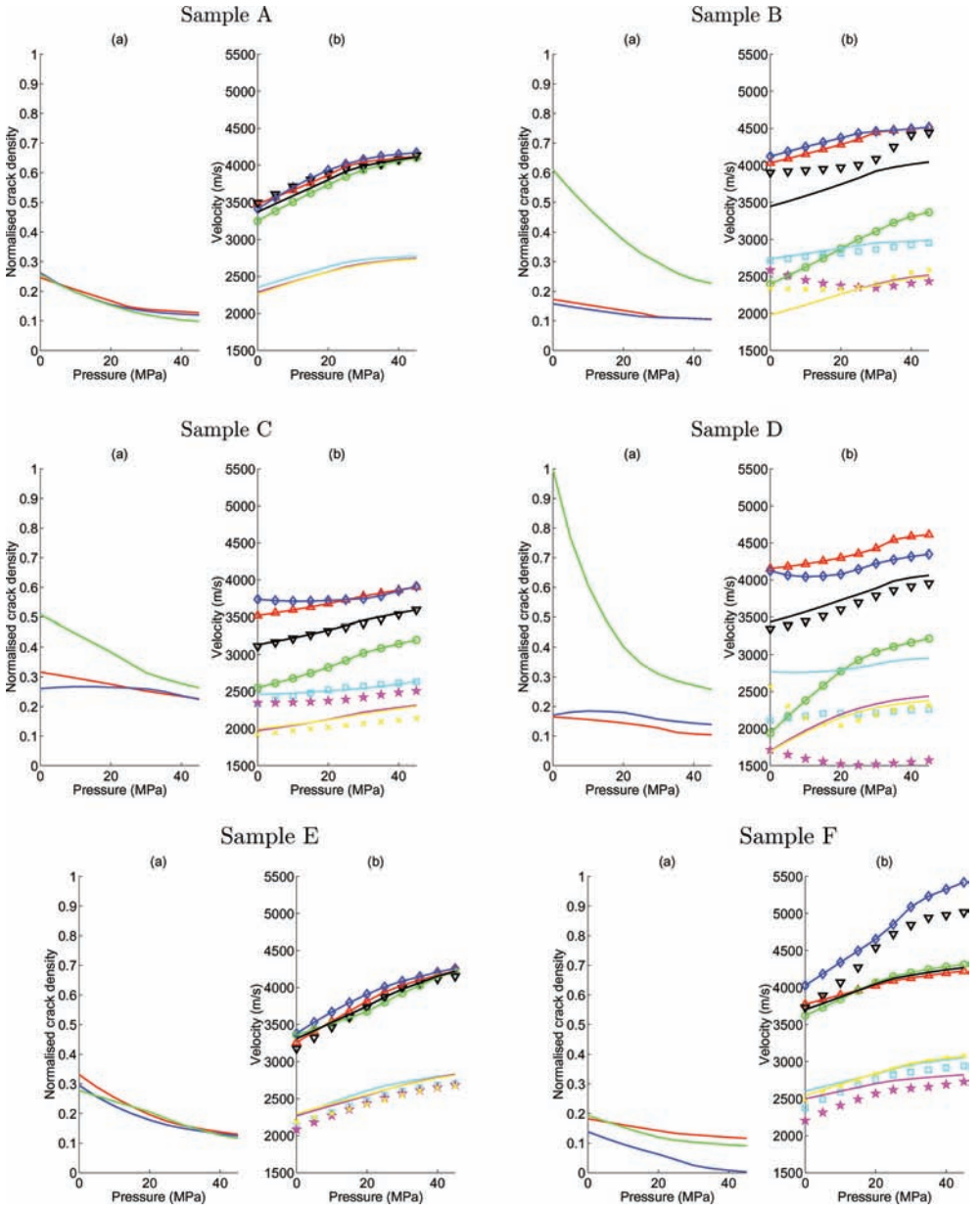

Figure 5. Inverted scalar crack densities (from using just the *P*-wave velocity data) and backcalculated velocities for samples A-I: (a) α_{ij} as a function of pressure calculated using just the *P*-wave velocity data for the three principal directions (red – α_{11}, blue – α_{22} and green – α_{33}). (b) Velocity data (symbols) and backcalculated velocities (lines) corresponding to the calculated α_{ij}s. (Green – v_{p33}, red – v_{p11}, blue – v_{p22}, black – $v_{p13}^{45^\circ}$, cyan – v_{s12}, magenta – v_{s13} and yellow – v_{s23}.)

related to the deviations from a scalar-crack model, misalignment of the principal axes of the anisotropy and the measurements or, perhaps, poorer data quality relating to obliquely cutting through the core.

4.2 Step 2: Perturbation analysis for β_{ijkl} (assuming α_{ij} fixed from step 1)

Fig. 7 shows the inverted α_{ij} and β_{ijkl} for samples *C* and *E*, respectively. Only these two samples are considered as these are the better quality data, and results for the other samples were less well determined. Additionally, sample *E* is the one that was 'washed out' and so the effects of this cleaning could possibly be assessed relative to the uncleaned sample *C*. The significance of β_{ijkl} is that it can provide insight into deviations from the scalar crack model and the ratio of B_N/B_T, which in turn may indicate something about the nature of the interfacial contacts of the cracks/grains. The observations for these two samples and the β_{ijkl} inversion are summarized below.

Sample C: Inclusion of the β_{ijkl} in general leads to an improved fit of all the velocity data and the backcalculated values with respect to the scalar-crack model. In particular, v_{s13} is much improved although there are still residual differences and this improvement is at the expense

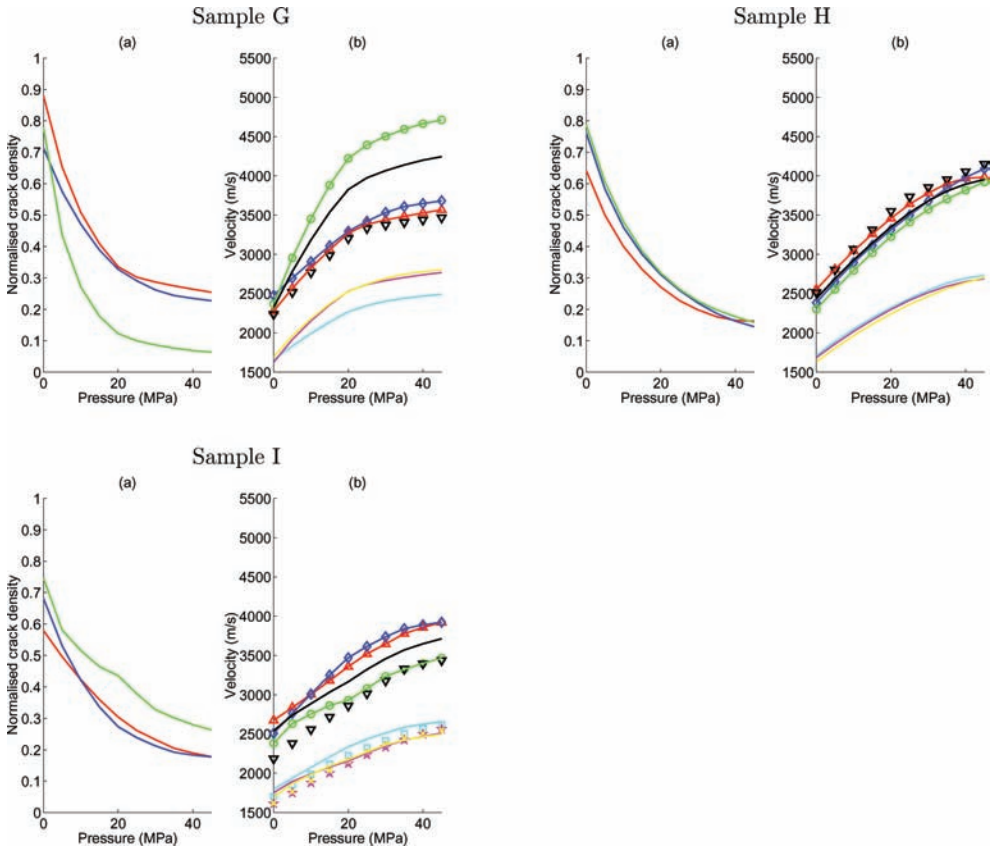

Figure 5. (*Continued.*)

of a slight degradation in the fit for $v_{p13}^{45^\circ}$. The magnitudes of the fourth-order tensor components are much smaller than the values of α_{ij}, with the exception of β_{1133}, which, though smaller than the α_{ij} values, is relatively large. Interpretation of the β_{ijkl} tensor is not as straightforward as for the scalar-crack model, but importantly two of the principal components, β_{1111} and β_{3333}, are positive, indicating that the effective crack sets with normals in x_1 and x_3 (the latter being horizontal cracks) and have values of $B_N > B_T$; this is most significant for the horizontal cracks at low pressure but $\beta_{1111} \approx \beta_{3333}$ at higher pressure. The other principal component, β_{2222}, starts slightly negative but is effectively zero, which indicates that $B_N \approx B_T$ for this set of fractures.

Sample E: Generally lower values of β_{ijkl} are found for this sample but the velocity fits are improved although $v_{s_{13}}$ is again less well-defined. In this case, all three principal components, β_{1111}, β_{2222} and β_{3333}, are negative suggesting that $B_N < B_T$, although these tend to zero ($\therefore B_N \approx B_T$) at higher pressure.

5 DISCUSSION AND INTERPRETATION

5.1 Crack density magnitudes

Before discussing the details of these results, it is important to comment on the generally high values of crack densities obtained. First, it should be remembered that the crack density referred to here encompasses the contributions of all the compliant anisotropic components not accounted for by the LPO + equant porosity calculation, that is, microcracks, thin pores, grain boundaries (including those filled with material that is more compliant than the grains themselves). However, the values of crack density presented here are larger than those typically found in the literature. The key difference between this work and most previous approaches is that, here, the total mismatch between the intrinsic anisotropic-LPO + equant porosity elasticity and the measured velocities is determined, whereas elsewhere the former is not known and the high-pressure asymptote is used as a proxy for the rock matrix with complete crack closure. However, is the high-pressure velocity asymptote really indicative of total crack closure? In fact this is not likely. What is more likely is that the high pressure velocity asymptote occurs when the grains have achieved a stable, strong configuration, in which there will be cracks that remain (partially) open because the grains are not intergrown and, therefore, do not perfectly tessellate. Furthermore there is likely to be in-filling material that further prevents crack closure. For these reasons, the high pressure asymptote will rarely indicate total crack closure for sandstones, at least, and thus estimates of crack densities based on the high-pressure velocity asymptote will likely be underestimates. It should also be noted that under hydrostatic loading this stable grain configuration will likely have more open cracks than would be seen under deviatoric loading, as there is less freedom for reorganization of the grains.

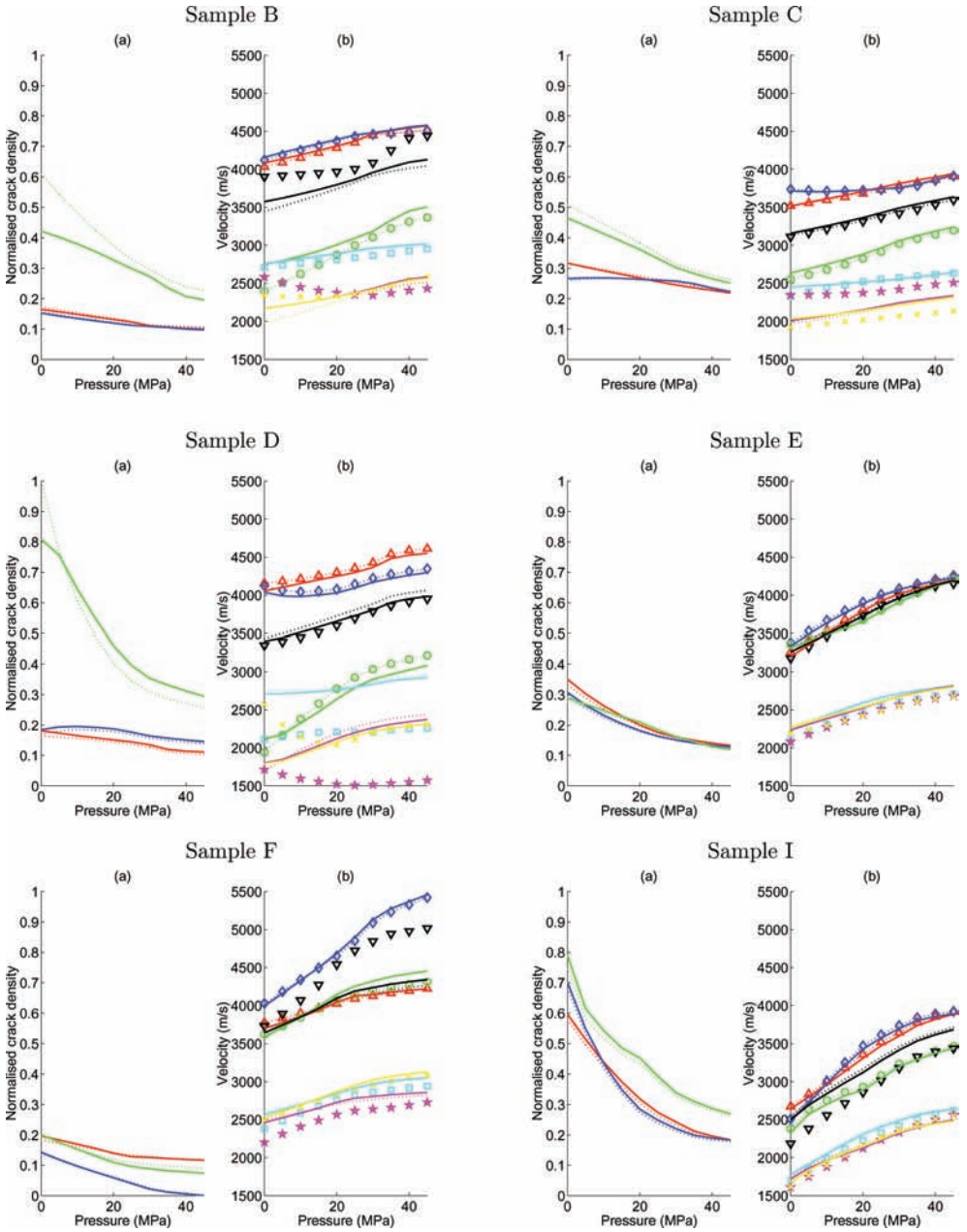

Figure 6. Inverted scalar crack densities (from using all velocity data) and backcalculated velocities for samples B, C, D, E, F and I: (a) α_{ij} as a function of pressure calculated using all velocity data (red – α_{11}, blue – α_{22} and green – α_{33}). (b) Velocity data (symbols) and backcalculated velocities (lines) corresponding to the calculated α_{ij}s (Green – $v_{p_{33}}$, red – $v_{p_{11}}$, blue – $v_{p_{22}}$, black – $v_{p_{13}}^{45^\circ}$, cyan – $v_{s_{12}}$, magenta – $v_{s_{13}}$ and yellow – $v_{s_{23}}$). The dotted lines are the results from the inversion using just the *P*-wave data as presented in Fig. 5.

It is important to note the inclusion of the background porosity in the calculations. In this work the total porosity was determined for each sample using mercury impregnation. These values were included as an isotropic term in the calculation of the 'LPO' background elasticities (i.e. this total porosity was assumed, in the calculation, to be equant (isotropic) pore-space). Any error in the quantification of the total porosity value would influence the crack density tensor only in an isotropic sense. For example, if the porosity had been underaccounted for (i.e. if there is more porosity than has been included in the background model), a larger difference between the observed high-pressure velocity asymptote and the LPO-based prediction would be observed, leading to an over-estimate of the overall crack density (i.e. giving an equal increase in α_{11}, α_{22} and α_{33}). However, the error in the measured total porosity value is not expected to be sufficiently large so as to be the origin of the high crack densities stated, that is, the high crack densities returned by the inversion are assumed to be real. Finally, it should also be noted that, any anisotropic aspect to the measured total porosity is captured by the crack density tensor, this includes deviations from 'equanticity' of the larger pores as well as the cracks and grain boundaries, etc., because the approach attributes all deviations of the velocity measurements from the background model to the crack density tensor. This is fully consistent with the previously stated definition of the crack-density tensor, that is, it encompasses all the contributions from all components of the anisotropic grain-scale porosity.

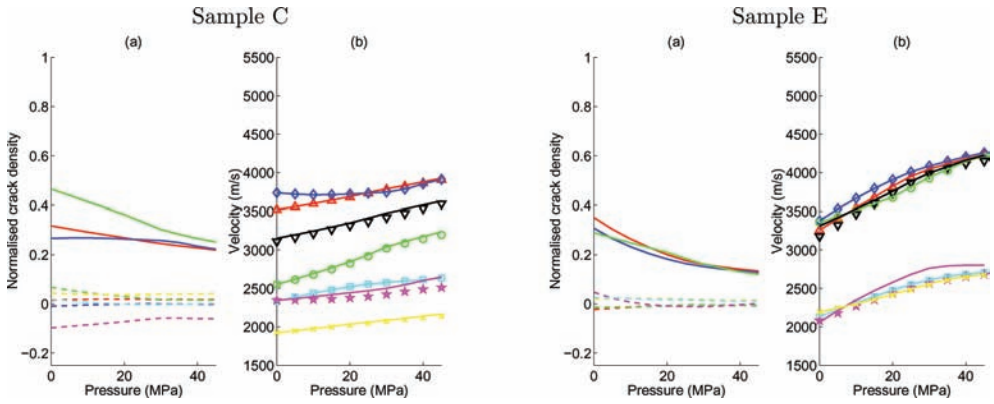

Figure 7. Inverted second and fourth order crack density tensor components and backcalculated velocities for samples C and E: (a) α_{ij} and β_{ijkl} as a function of pressure calculated using all velocity data (solid lines, α_{ij}: red – α_{11}, blue – α_{22}, green – α_{33}; dashed lines, β_{ijkl}: red – β_{1111}, blue – β_{2222}, green – β_{3333}, yellow – β_{2233}, magenta – β_{1133} and cyan – β_{1122}). (b) Velocity data (symbols) and backcalculated velocities (lines) corresponding to the calculated α_{ij}s. (Green – $v_{p_{33}}$, red – $v_{p_{11}}$, blue – $v_{p_{22}}$, black – $v_{p_{13}}^{45^\circ}$, cyan – $v_{s_{12}}$, magenta – $v_{s_{13}}$ and yellow – $v_{s_{23}}$.)

Table 2. Summary of observations from velocity versus pressure and associated inverted scalar crack density tensor components.

Sample	Velocities	Scalar crack density tensor	Observations
A	VTI → isotropic	≈ Isotropic	Slightly reduced horizontal cracking (α_{33}) at higher pressures but low crack (and velocity) anisotropy.
B	VTI	VTI (very large α_{33})	Large pressure-dependence of α_{33}. At low pressures slight difference in α_{11} and α_{22}. Variation of shear velocities and v_p^{45} with pressure is not matched by the backcalculation; suggests significant β_{ijkl} terms and variation of $B_N{:}B_T$ with loading.
C	Orthorhombic → VTI	Orthorhombic ($\alpha_{33} > \alpha_{11} > \alpha_{22}$) → VTI	Good velocity fits, except for the vertical shear waves. Moderate pressure-sensitivity for α_{33} and less for the other crack sets.
D	VTI → orthorhombic ($v_{p_{33}} \ll v_{p_{22}} < v_{p_{11}}$)	Strong VTI → orthotropic ($\alpha_{33} > \alpha_{22} > \alpha_{11}$)	Complicated velocity pressure-dependence. Large α_{33} (especially at low pressure); strong pressure sensitivity. Poor shear velocity fits.
E	≈ Isotropic	≈ Isotropic	Variation of α_{33} with pressure is markedly different to the other two crack densities – higher horizontal crack densities at intermediate pressures indicating that these cracks are harder to close (less compliant) than the vertical cracks.
F	Fast $v_{p_{22}}$ and $v_{p_{13}}^{45^\circ}$	≈ Orthotropic → HTI ($\alpha_{33} > \alpha_{11} > \alpha_{22} \rightarrow \alpha_{33} \approx \alpha_{11} > \alpha_{22}$)	Highly deviated (fast) $v_{p_{13}}^{45^\circ}$, which is closer to $v_{p_{22}}$ than $v_{p_{11}}$ or $v_{p_{33}}$. Dipping cracks oriented with normals in the x_1x_3 plane?
G	At higher pressure: $v_{p_{33}} \gg v_{p_{11}} \approx v_{p_{22}}$	Initially orthotropic ($\alpha_{11} > \alpha_{33} > \alpha_{22}$), generally CTI ($\alpha_{11} \approx \alpha_{22} > \alpha_{33}$	Anisotropy increases with pressure. All the crack sets show a strong pressure sensitivity. Distribution of vertical cracks with their normals distributed in the x_1x_2 plane (CTI)?
H	Weak orthorhombic	HTI ($\alpha_{11} \ll \alpha_{22} \approx \alpha_{33}$) →≈ isotropic	$v_{p_{13}}^{45^\circ} \approx v_{p_{11}}, v_{p_{22}}$. All components of α_{ij} show significant pressure-dependence.
I	Orthotropic → VTI	Orthotropic → VTI ($\alpha_{33} \gg \alpha_{22} \approx \alpha_{11}$)	$v_{p_{13}}^{45^\circ}$ is similar to $v_{p_{33}}$ and $v_{s_{23}} \approx v_{s_{13}} < v_{s_{12}}$. All crack sets have strong pressure sensitivity.

5.2 Interpretation of crack density tensors

The first key observation that can be made from the preceding results is that the velocity anisotropy and crack anisotropy symmetries are similar and also that the crack densities do not tend to zero for higher pressures. This indicates that the principal grain-scale source of anisotropy is due to the grain-boundary cracks with a lesser effect from intrinsic LPO. However this observation also suggests that the intrinsic and extrinsic anisotropies are linked, which could be because the grain alignment controls both the LPO (crystal axis orientation) and grain-boundary SPO (grain boundary alignment will clearly be related to the grain orientations for non-isotropic grain shapes). However, including the LPO effects in the inversion does seem to be necessary to properly assess the extrinsic anisotropy, as can be seen by comparing the velocity and the crack density plots.

The second key observation is that, the observed non-LPO anisotropy can be considered to be structural, that is, due to the architecture of the grain boundaries and cracks and is load-dependent. It does not however appear to be load-induced. This distinction is important since any interpretation of so-called stress-induced anisotropy, either from such laboratory data or from field-scale seismic data, will be heavily influenced by this non-isotropic load-dependent structural anisotropy.

In general, the scalar-crack model provides reasonable results, particularly at higher pressures, so good insight might be gained from just the α_{ij} crack density inversion results. Observed deviations indicate there is an influence due to the fourth-order tensor terms, but this is

small. Therefore, it seems reasonable to have assumed $B_N = B_T$ in the initial stage of the inversion and to have subsequently assessed the β_{ijkl} as a perturbation to the scalar-crack model.

From the α_{ij} results, it is seen that, for these samples, there is generally much less vertical cracking than horizontal. Furthermore there is little preferential alignment of the vertical cracking that does exist (usually at lower pressures). This indicates a general lack of directional-flow-deposition or vertically aligned damage fabrics. Thus the extrinsic anisotropies, that is, the grain-boundary architectures, seem to be largely related to simple depositional fabrics (in general VTI). Sample *F* is a slight exception to this, as it shows a highly deviated (fast) $v_{p13}^{45^\circ}$, which is closer to v_{p22} than v_{p11} or v_{p33}. This perhaps indicates that in fact there are dipping cracks oriented with normals in the x_1x_3 plane. If the angle of this crack-plane were approximately 45° it would lead to a faster $v_{p13}^{45^\circ}$, close to v_{p22}, and $\alpha_{33} \approx \alpha_{11}$, as observed. This dipping fabric would probably be related to depositional cross-bedding with a flow direction roughly parallel to x_2. Sample *G* is the only case with significantly more vertical cracking than horizontal and seems to have a CTI crack assemblage (CTI, circular transverse isotropy, refers to the case where all the cracks are aligned with their normals randomly distributed but in the same plane); this is discussed further below. Sample *D* is also anomalous in that at higher pressure it is orthotropic with $\alpha_{33} > \alpha_{22} > \alpha_{11}$, which suggests a preferential direction of cracking. With the current data and analysis, the crack density tensors for these anomalous cases can not be properly assessed since the principal axes of the anisotropy are likely not aligned with the velocity measurements. However, it is interesting to note that the backcalculations of $v_{p13}^{45^\circ}$, for sample *D*, are not far off the data values, which suggests that the general model is reasonable, whereas for *G* the misfit is large.

Independent data, based on anisotropic magnetic susceptibility analysis of these samples (Hailwood 2004, personal communication), suggests that in general the main depositional flow direction was at roughly 45° to the x_1 and x_2 axes. Unfortunately, if such flow directionality has led to a grain-boundary alignment this will not be detected with the current data set, due to the lack of off-axis measurements in the *X*–*Y* plane. Additionally, this effect could lead to equal velocities along x_1 and x_2 (as seen in the *X*–*Z* plane for sample *F*), which would give an impression of isotropy in that plane. Similarly the apparent CTI symmetry in sample *G* could in fact be a set of cracks aligned in this sense (note also that this sample was cleaned prior to the analysis).

Deviations of the measured velocities from those backcalculated using the inverted α_{ij} values indicate some influence due to the fourth-order tensor terms. For one of the samples considered in the inversion for β_{ijkl} (sample *C*), it appears that $B_N > B_T$ for both the horizontal crack-set and the vertical crack-set with normals parallel to x_1 (for the other effective crack-set $\beta_{2222} \approx 0$ so $B_N \approx B_T$). This suggests that the two non-scalar crack-sets are more compliant in crack-normal displacements than in shear; this is contrary to the results of Sayers (2002). However for the other sample considered for β_{ijkl} (sample *E*) it is observed that β_{1111}, β_{2222} and β_{3333} are negative suggesting that $B_N < B_T$ for all the effective crack-sets. Additionally, it is noted that the magnitudes of the α_{ij} values are generally smaller for sample *E* compared to *C*; this suggests lower B_T values for sample *E*. Sample *E* was washed-out prior to the analysis, thus it appears that cleaning might reduce the crack compliances with particular impact on the normal compliance (generally, the cleaning appeared to remove much of the organic, hydrocarbon, products, but perhaps also fine clays and materials which propped open cracks). The data used by Sayers (2002), which showed negative principal β_{ijkl} values ($B_N < B_T$), were for a clean sandstone from a surface outcrop (Penrith), thus it might be concluded that clean(ed) sandstones show $B_N < B_T$ whilst reservoir sandstones may have $B_N > B_T$. Furthermore the observed effect of the cleaning suggests that the cracks in sample *C* were likely present *in situ* as extraction-induced cracks would not contain the organic material that appears to cause B_N to be larger than B_T. However without comparison of the same samples before and after cleaning strong conclusions based on these observations are difficult.

Commonly the alignment of highly anisotropic mica crystals can produce strong anisotropy in a rock. Fig. 8 presents the variation in observed anisotropy versus the modal content of mica in each sample plus how the different contributions to this anisotropy (i.e. crack- or LPO-induced and total anisotropies) vary with mica content. Similar analysis has been carried out for the other constituent minerals but significant trends were only observed for the micas. The important observations from Fig. 8 are summarized below.

A general increase in the measured anisotropy with increasing mica content is observed at 0 MPa for the *x*–*z* and *y*–*z* *P*-wave anisotropies, but not for the *y*–*z* anisotropy (Figs 8a and b). The low mica-content samples show an increase in anisotropy with loading such that at 45 MPa they have almost equivalent anisotropy to the high mica content samples. Therefore, the trend with increasing mica content is less apparent at high pressure. However, the low mica samples do not have a consistent symmetry and, in general, as the mica content increases the samples become more VTI and the magnitude of this VTI anisotropy increases with mica content; this is both in terms of LPO and crack anisotropies. In Fig. 8(c) it can be seen that the LPO anisotropy increases with mica content (for the difference between horizontal and vertical propagation, but there is no real change in anisotropy in *x*–*y* plane). However, this anisotropy is much less than that observed in the velocity data. Therefore, there must also be a significant contribution to the anisotropy from cracks associated with the flat mica grains (e.g. intergranular cracks, grain boundaries or cracking along cleavage planes). Fig. 8(d) shows that the low mica content samples have high crack densities at 0 MPa but the three crack densities are approximately equal (indicating roughly isotropic cracking). For the higher mica content samples there is an increase in horizontal crack densities (α_{33}) with mica content; this trend is reduced with loading, but at 45 MPa there is still a general increase in horizontal cracks with mica content. The effects of these trends in crack densities on the expected velocity anisotropy are shown in Figs 8(e) and (f). These figures show that the velocity anisotropy due to just cracks has a strong increasing trend with increasing mica content for the *x*–*z* and *y*–*z* values, but not for the *x*–*y* anisotropies. This trend may exist at higher pressure although the low mica samples also have high anisotropies at high pressure. However, as noted previously, these low-mica samples do not have a consistent symmetry, whilst it appears that the VTI crack-induced anisotropy increases with mica content.

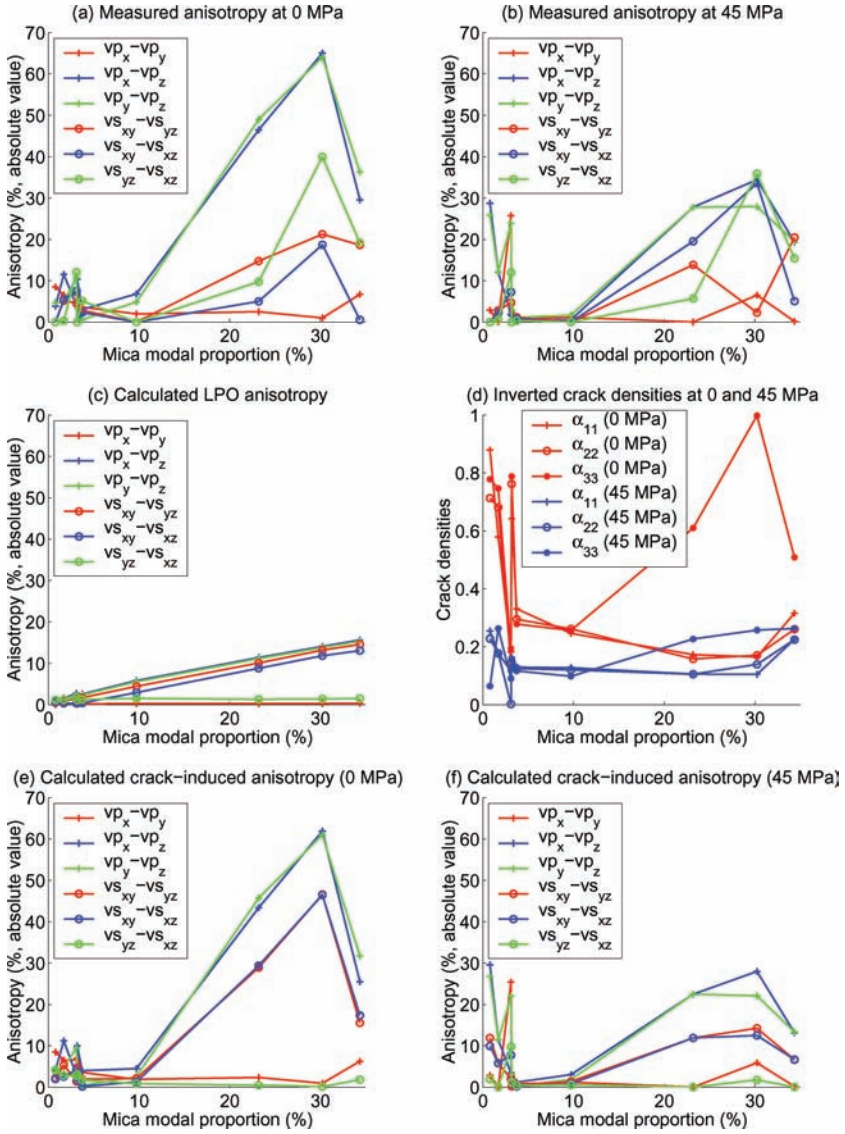

Figure 8. Anisotropy versus mica content. (a) and (b) total (measured) velocity anisotropies for 0 and 45 MPa, respectively. (c) Calculated LPO-induced velocity anisotropies based on the EBSD measurements. (d) Scalar crack densities (α_{ij}) inverted from velocity data (using just *P* waves). (e) and (f) Velocity anisotropy due to just cracks (i.e. based on stiffnesses derived by adding the inverted crack densities, α_{ij}, to the Voigt–Reuss–Hill average isotropic elasticities). In each case the values are plotted versus mica content such that they appear in order of increasing mica content from left to right: G, I, F, H, E, A, B, D and C (see Fig. 3).

In summary, the results in Fig. 8 indicate that micas contribute an anisotropic effect to the elastic properties through their LPO, but also have a strong influence on the cracking; this is likely representative of increased cracking parallel to the flat mica grains or their cleavage planes.

Finally, whilst the pressure-dependence of the anisotropy has not been explicitly treated, the results, the measurements and subsequent crack-density tensor inversions for a range of pressures provide insight into the pressure-sensitivity of these rocks. Future work will consider the inversion of the data as a function of pressure, rather than at discrete pressure levels, for example, following the work of Toksoz *et al.* (1976). However this likely involves assuming some idealized crack shape, for example, penny-shaped or ellipsoidal, which thus far (other than the normalizing factor *h*) has been avoided.

5.3 Implications for reservoir characterization, monitoring and anisotropy analysis

The presented analysis has provided a characterization of the core samples in terms of their crack distribution (separated from the LPO contribution). As discussed above, these crack distributions essentially relate to the architecture of the compliant grain contacts due mainly to depositional features and to a lesser extent damage (the origin of the latter may be open to question, *in situ* or during core extraction/preparation, and so may not be relevant *in situ*). In terms of the reservoir characterization, these results provide a clear indication of the grain-scale contributions to the elastic anisotropy, and their load dependence. Any interpretation of anisotropy at the field scale, must first take into account

this grain-scale anisotropy. One can then have much more confidence in interpreting the larger scale anisotropy, such as that associated with reservoir-scale fractures.

The presented results (or equivalent results for other fields derived by this method) might be used to reduce the non-uniqueness of the interpretation of reservoir seismic data. This would first involve determing what anisotropy might be expected due solely to the grain-scale contributions then attributing the remainder to larger-scale contributions, such as fracturing. In particular, as the observed anisotropies are in this case generally close to isotropic or VTI (or dipping VTI) at higher pressures, it seems that any azimuthal anisotropy observed *in situ* (e.g. using azimuthal amplitude/traveltime or shear wave splitting analyses) would most likely be due to larger-scale contributions such as vertical fracturing. However, samples *G*, *H* and *I*, from the deeper cleaner sandstone units, show stronger pressure sensitivity for all components of α_{ij}, which suggests that under anisotropic loading these units could exhibit some load-induced azimuthal anisotropy. Such induced anisotropy might be detected *in situ* and thus complicate the interpretation for fractures; in this case the laboratory data could be used to provide bounds on the load-induced anisotropy and thus on the inferences for fracture contributions.

Other than potentially aiding the interpretation of seismic anisotropy for fracture characterization, the results also suggest there is potential for using non-hyperbolic moveout analysis to assess, in a time-lapse sense, changes in effective stress, as the pressure sensitivity is generally greatest for the horizontal crack sets. This potential is greatest for the mica-rich units (samples *B*, *C* and *D*).

An alternative use of these data is in the prediction of crack-densities at any reservoir pressure, for example, for known *in situ* conditions or for pressures in a model simulation. Such predictions could thus be used in reservoir flow simulations.

It should be noted that the response to loading of these rocks *in situ* would vary from the observed loads in the laboratory, but how is difficult to assess. For example, is hydrostatic loading appropriate? Probably not. The influence of fluids and/or clays has also been neglected. It is likely that under deviatoric loads a different response will be observed, which includes the fact that the damage threshold will be much lower for deviatoric loads than for hydrostatic loading. Therefore, direct use of the quantified load-dependence of the velocities and/or crack density tensors is only appropriate in circumstances where there is no deviatoric loading. However, below the damage threshold it is possible that the observed load-dependences can be used as a guideline in terms of identifying which zones are likely to be more pressure sensitive and also to infer *in situ* stresses or crack densities based on measured velocity anisotropies.

6 CONCLUSION

This work has considered the quantification of the different grain-scale contributions to the elastic anisotropy in core samples from a UKCS oil field using multi-axial ultrasonic data and petro-fabric analyses. Such insight provides constraints on the contributions of grain-scale LPO and load-dependent SPO to the overall observed anisotropy that might be incorporated into the interpretation of field-scale seismic data.

The approach of Sayers (2002), for determining second- and fourth-order crack density tensors, has been extended to allow the use of all available ultrasonic *P*- and *S*-wave data, to consider an orthorhombic background medium and also to permit a greater number of components of β_{ijkl} to be assessed. A key development is the integration of a known intrinsic (LPO) anisotropy into the analysis by an extension of the underlying equations. This extension allowed estimates of the extrinsic anisotropy, that is, the quantified crack density tensors, that are 'unpolluted' by the contributions from the intrinsic anisotropy, therefore, the extrinsic and intrinsic anisotropies can be distinguished.

The results show that, for the samples considered, the extrinsic crack-induced anisotropy is strong relative to that of the intrinsic LPO effects and that, in general, the predominant crack-set in these samples is aligned parallel to the depositional fabric (generally horizontal). It is, however, observed that the LPO and extrinsic anisotropies are often aligned, which indicates that they are likely linked in origin; the obvious explanation being that the cracks are related to the grain-boundary contacts, which are aligned with the grains (which also provide the LPO). In particular, there is a strong link between the degree of anisotropy and the modal content of micas, which can not be explained solely by the LPO effect. Thus, in addition to a strong LPO effect, the micas are also associated with increased horizontal (grain parallel) crack densities, which enhances the overall VTI velocity anisotropy.

Analysis of the fourth-order crack density tensor has allowed some insight into the relative sizes of the normal and tangential crack compliances, B_N and B_T. For one case the inverted fourth order terms suggest $B_N \geq B_T$, that is, the crack are more compliant in compression than in shear. However, for another sample, which had been cleaned prior to the analysis (leading to the removal of much of the organic, and perhaps fine clay, material) the results suggest $B_N < B_T$, that is, the cracks are more compliant in shear than compression. This observation may have significant implications for the use of analogue samples acquired at the surface where crack filling material, which might lead to reduced shear compliances, are not present.

ACKNOWLEDGMENTS

This work was carried out within context of the Seismic Anisotropy as an Indicator of Lithology (SAIL) project under the Structurally Complex Reservoirs framework brokered by the Industry Technology Facilitator (ITF) and sponsored by AmeradaHess, BG Group, BP, Chevron-Texaco, Kerr-McGee, Shell, Total and the UK-DTI. SH was supported by a Marie Curie Intra-European Individual Fellowship, at Laboratoire 3S (Grenoble, France), within the 6th European Community Framework Program (project, iGEM). Thanks to Steve Covey-Crump and Walid Ben Ismail (University of Manchester) for the ultrasonic data measurements and to the oilfield owners for providing access to core and for permission to publish the results. Thank you also to the two anonymous reveiwers and the editor, Dr Yehuda Ben-Zion, for their helpful feedback.

REFERENCES

Blackman, D.K. & Kendall, J.-M., 1997. Sensitivity of teleseismic body waves to mineral texture and melt in the mantle beneath a mid-ocean ridge, *Phil. Trans. Roy. Soc. Lond., A,* **355,** 217–231.

Budiansky, B. & O'Connell, R., 1976. Elastic moduli of a cracked solid, *Int. J. Solids Struct.,* **12,** 81–97.

Cholach, P. & Schmitt, D., 2003. Seismic anisotropy of shales, *CSEG Recorder,* **28,** 39–42.

Crampin, S., 1984. Effective anisotropic elastic constants for wave propagation through cracked solids, *Geophys. J. R. astr. Soc.,* **76,** 135–145.

Debski, W. & Young, R.P., 1999. Enhanced velocity tomography: practical method of combining velocity and attenuation parameters, *Geophys. Res. Lett.,* **26,** 3253–3256.

Gueguen, Y. & Schubnel, A., 2003. Elastic wave velocities and permeability of cracked rocks, *Tectonophysics,* **370,** 163–176.

Hall, S., Kendall, R., Kendall, J.-M. & Sondergeld, C., 2000. Analysis of anisotropic velocities in a core sample and AVOA from a fractured vuggy carbonate reservoir, in *Anisotropy 2000: Fractures, Converted Waves, and Case Studies*, Tulsa, USA, pp. 257–269, Society of Exploration Geophysists.

Han, J., Schmitt, D., Collis, D. & Escartin, J., 2004. Laboratory determination of velocity anisotropy, in *Proceedings of the 2004 CSEG National Convention*. Canadian Society of Exploration. *Geophysics,* Calgary, Canada.

Hillier, S., 1999. Use of an air-brush to spray dry samples for X-ray powder diffraction, *Clay Miner.,* **34,** 127–135.

Hoenig, A., 1978. Elastic moduli of a non-randomly cracked body, *Int. J. Solids Struct.,* **15,** 137–154.

Hornby, B., 1998. Experimental laboratory determination of the dynamic elastic properties of wet, drained shales, *J. geophys. Res.,* **103**(B12), 29 945–29 964.

Hudson, J., 1980. Overall properties of a cracked solid, *Math. Proc. Camb. Phil. Soc.,* **88,** 371–384.

Hudson, J., 1981. Wave speeds and attenuation of elastic waves in material containing cracks, *Geophys. J. R. astr. Soc.,* **64,** 133–150.

Hudson, J. & Liu, E., 1999. Effective elastic properties of heavily faulted structures, *Geophysics,* **64,** 479–485.

Kachanov, M., 1980. Continuum model of medium with cracks, *J. Eng. Mech. (ASCE),* **106,** 1039–1051.

King, M., Chaudhry, N. & Shakeel, A., 1995. Experimental ultrasonic velocities and permeability for sandstones with aligned cracks, *Int. J. Rock Mech. Mining Sci.,* **32,** 155–163.

Lo, T., Coyner, K. & Toksoz, M., 1986. Experimental determination of elastic anisotropy in Berea sandstone, *Geophysics,* **51,** 164–171.

Maddock, J., Fisher, Q., Kendall, J.-M. & Lloyd, G., 2004. Petrofabric analysis of seismic anisotropy in siliciclastic sedimentary rocks, in 66th Meeting, EAGE, Extended Abstracts, E11.

Mainprice, D., 1990. An efficient FORTRAN program to calculate seismic anisotropy from the lattice preferred orientation of minerals, *Comput. Gesosci.,* **16,** 385–393.

Nur, A., 1971. Effects of stress on velocity anisotropy in rocks with cracks, *J. geophys. Res.,* **76,** 2022–2034.

Nur, A. & Simmons, G., 1969. Stress-induced velocity anisotropy in rock: an experimental study, *J. geophys. Res.,* **74,** 6667–6674.

Press, W., Flannery, B., Teukolsky, S. & Vetterling, W., 1992. *Numerical Recipes in FORTRAN*, 2nd edn, Cambridge University Press, New York, NY, USA.

Rasolofosaon, P., 1998. Stress-induced seismic anisotropy revisited, *Rev. Inst. Franc. Petr.,* **53,** 679–692.

Rasolofosaon, P., Rabbel, W., Siegesmun, S. & Vollbrecht, A., 2000. Characterization of crack distribution: fabric analysis versus ultrasonic inversion, *Geophys. J. Int.,* **141,** 413–424.

Sayers, C., 2002. Stress-dependent elastic anisotropy of sandstones, *Geophys. Prospect.,* **50,** 85–95.

Sayers, C. & Kachanov, M., 1991. A simple technique for finding effective elastic constants of cracked solids for arbitrary crack orientation statistics, *Int. J. Solids Struct.,* **27,** 671–680.

Sayers, C. & Kachanov, M., 1995. Microcrack-induced elastic wave anisotropy of brittle rocks, *J. geophys. Res.,* **100,** 4149–4156.

Schoenberg, M. & Sayers, C., 1995. Seismic anisotropy of fractured rock, *Geophysics,* **60,** 204–211.

Stanchits, S., Lockner, D. & Ponomarev, A., 2003. Anisotropic changes in *P*-wave velocity and attenuation during deformation and fluid infiltration of granite, *Bull. seism. Soc. Am.,* **93,** 1803–1822.

Toksoz, M.N., Cheng, C.H. & Timur, A., 1976. Velocities of seismic waves in porous rocks, *Geophysics,* **45,** 621–645.

Valcke, S., Casey, M., Lloyd, G., Kendall, J.-M. & Fisher, Q., 2006. Lattice preferred orientation and seismic anisotropy in sedimentary rocks, *Geophys. J. Int.,* **166,** 652–666.